Biodegradation by cancer cells of magnetite nanoflowers with and without encapsulation in PS-b-PAA block copolymer micelles

Emilia Benassai, Niéli Daffé, Elif Aygun, Audrey Geeverding, Emine Ulku, Claire Wilhelm, Ali Abou-Hassan

Biodegradation by cancer cells of magnetite nanoflowers with and without encapsulation in PS-b-PAA block copolymer micelles

Emilia Benassai [a], Niéli Daffé [b], Elif Aygun [c], Audrey Geeverding [d], Emine Ulku Saritas [c,e], Claire Wilhelm [f], Ali Abou-Hassan [a,g,*]

[a] Sorbonne Université, CNRS, Physicochimie des Électrolytes et Nanosystèmes InterfaciauX (PHENIX), F-75005 Paris, France.

[b] Swiss Light Source, Paul Scherrer Institut, 5232, Villigen, Switzerland

[c] Department of Electrical and Electronics Engineering, Bilkent University, Ankara, Turkey, 06800

[d] Sorbonne Université, CNRS, Institut de Biologie Paris-Seine (IBPS), Service de microscopie électronique (IBPS-SME), F-75005, Paris

[e] National Magnetic Resonance Research Center (UMRAM), Bilkent University, Ankara, Turkey, 06800

[f] Laboratoire Physico Chimie Curie, Institut Curie, CNRS, PSL Research University, Paris, France

[g] Institut Universitaire de France (IUF), 75231 Cedex 05, Paris, France

Keywords

Magnetic nanoparticles; PS-b-PAA block copolymer; Magnetic micelles, Biodegradation; Cancer cells spheroids

Abstract

Magnetomicelles were produced by the self-assembly of magnetite iron oxide nanoflowers and the amphiphilic poly(styrene)-b-poly(acrylic) acid block copolymer to deliver a multifunctional theranostic agent. Their bioprocessing by cancer cells was investigated in a three-dimensional spheroid model over a 13-day period, and compared with non-encapsulated magnetic nanoflowers. A degradation process was identified and monitored at various scales, exploiting different physicochemical fingerprints. At a collective level, measurements were conducted using magnetic, photothermal, and magnetic resonance imaging techniques. At the nanoscale, transmission electron microscopy was employed to identify the morphological integrity of the structures, while X-ray absorption spectroscopy was used to analyze the degradation at the crystalline phase and chemical levels. All these measurements converge to demonstrate that the encapsulation of magnetic nanoparticles in micelles effectively mitigates their degradation compared to individual non-encapsulated magnetic nanoflowers. This protective effect consequently resulted in better maintenance of their therapeutic photothermal potential. The structural degradation of magnetomicelles occurred through the formation of an oxidized iron phase in ferritin from the magnetic nanoparticles, leaving behind empty spherical polymeric ghost shells. These results underscore the significance of encapsulation of iron oxides in micelles in preserving nanomaterial integrity and regulating degradation, even under the challenging physicochemical conditions within cancer cells.

1. Introduction

Due to their multifunctional properties, iron oxide nanoparticles remain potent nanomaterials for the biomedical field. In addition, their biocompatibility makes them promising theranostics for biomedical applications. Thanks to their intrinsic magnetic properties, they can be manipulated and activated at a distance using magnetic fields,[1-5] enabling numerous applications such as imaging, triggered drug delivery, magnetic hyperthermia, magnetic targeting, and manipulation.[6-10]

Besides, in addition to their magnetism, magnetite iron oxides possess interesting optical features in therapeutic near-infrared (NIR) biological windows. When submitted to photo-stimulation they can convert light to heat which can be used for biomedical photothermia (PT) such as in cancer therapy. [6, 11-13] Polyol-synthesized magnetite iron oxide nanoflowers (IONFs) are to date among the best efficient magnetic nanoparticles for thermal therapies, with excellent photothermal performance in the therapeutic windows.[12, 14] Their synthesis process and photothermal heating have been demonstrated and rationalized. [14-18]

Upon their interaction with cells and encapsulation in endosomes nanoparticles can undergo structural modifications that can affect their properties and their ability to perform their programmed tasks.[19, 20] Understanding the impact of confinement and cellular bioprocessing on the structure, properties and functions of nanomaterials in cells is crucial for designing efficient and sustainable nanomedicine. 3D cell spheroids offer a nice opportunity to study and track theranostics fate on different scales over time using diverse metrics.[21] They have provided valuable insights into the biodegradation of various nanomaterials, including optically active and magnetic ones.[22-24]

Recent reports on nano-theranostics have emphasized the role of the structure in modulating their biodegradation in solution, cells or *in vivo*.[19, 25] Different strategies have been explored including grafting of different types of ligands on their surface, encapsulation of the nanoparticles in organic shells such as imprinted porous polymers or inorganic silica shells.[11, 26-30] Amphiphilic block copolymers (BCP) are a class of polymers that have gathered lot of interest in materials

science due to their versatility to self-assemble into different nanostructures as potential nanocarriers.[31, 32] BCP can self-assemble with inorganic nanoparticles into hybrid nano-architectures of different functionalities while providing to the inorganic part a better stability, reduced toxicity, and protection from their environment.[32-36] Poly(styrene)-block-poly(acrylic acid) (PS-b-PAA) is one of the most extensively studied BCPs in the field of polymers. It has been explored for the co-assembly of various types of nanoparticles including magnetic nanoflowers motivated by the versatility and rigidity of the micelles due to PS.[36-39] To overcome the limitations related to the large-scale production of magnetic micelles encountered in bulk, we have recently developed a high throughput microfluidic strategy.[39] IONFs were encapsulated inside the polymeric PS and large scale of IONFs@PS-b-PAA magnetomicelles were produced. We showed that magnetomicelles are multifunctional theranostics with excellent photothermal functions when excited in the biosafe NIR-I-II window, in addition to being excellent T_2 contrast agents in magnetic resonance imaging (MRI) and imaging agents for magnetic particle imaging.

Given the promising theranostic functions of the magnetic micelles in solution and the physicochemical properties of the PS-b-PAA, it was evident to question whether the structural and functional integrities of the magnetomicelles are maintained once internalized in cells and consequently if the PS core could serve as a relevant strategy to modulate the bioprocessing of the inorganic core in cancer cells.

In this study, we investigated the degradation of IONFs@PS-b-PAA magnetic micelles in a three-dimensional spheroid cancer model. Employing a multi-scale physicochemical and materials science approach, we traced the fate of magnetomicelles and non-encapsulated IONFs across different length scales using a plethora of tools. These include physical macroscopic metrics such as magnetometry and photothermia, local metrics such as transmission electron microscopy (TEM) for the morphology, and X-ray absorption spectroscopy (XAS) for analyzing the local chemical crystalline structure, supplemented by magnetic resonance imaging (MRI). Overall, we demonstrate that the physicochemical conditions within cancer cell can overcome the plasticity of the PS core, leading to a mitigate degradation of the IONFs in the micelles. However, compared to non-encapsulated IONFs the degradation in the magnetomicelles was slowed down. Besides, despite bioprocessing and biodegradation causing a loss of structural integrity of the polymeric PS core, the magnetic nanoparticles retained sufficient photothermal heating capability over a 13-day timescale.

2. Materials and Methods

2.1 Chemicals

All the products listed are of analytical purity grade and they are used without further purification. Reagents and washing solvents are hydrochloric acid (HCl, 37%), nitric acid (HNO3, 68%), ammonia (NH3, 20%), ethanol (96%), acetone (>99%), diethyl ether (Et_2O, 100%), methanol (≥99.5%), all furnished by VWR International; trisodium citrate dihydrate ($C_6H_5Na_3O_7{\cdot}2H_2O$), oleic acid (>90%) and tetrahydrofuran anhydrous (THF, ≥99%) are supplied by Merck. The block copolymer polystyrene-b-poly(acrylic acid) (PS_{403}-b-PAA_{62}) is provided by Polymer Source, Inc (Canada). Microfluidic material is supplied by Cluzeau info labo (C.I.L., France) and consists of a cross stainless-steel micromixer (10-32 for inner tubing 10/16'', 0.040''), Teflon PFA tubing (10/16'', 0.040'') and a PEEK tubing (360 µm × 150 µm, 0.006''). Calcein-AM (≥ 95.0 %) is purchased from Merk, while glutaraldehyde (25%) is purchased from Agar Scientific. Paraformaldehyde (16%), sodium cacodylate trihydrate, osmium tetroxide (OsO_4, 4%), red Ruthenium powder, and EPON resin are obtained from Electron Microscopy Sciences (EMS). Oolong tea powder (O.T.E.) is purchased from Delta Microscopies (France), agarose powder (low melting point) is obtained from Promega (France). Uranyl acetate powder is purchased from Prolabo.

2.2 Synthesis of IONFs and their surface modification

The ferric (1.08 g, 4mmol) and ferrous (0.39 g, 2 mmol) precursors were mixed in 80 mL of a mixture of DEG and NMDEA (1:1, v/v), under nitrogen atmosphere to prevent iron (II) oxidation, and dissolved overnight. In parallel, sodium hydroxide was dissolved in 40 mL of the same DEG/NMDEA mixture under nitrogen atmosphere; the alkaline solution was added to the iron precursor solution under magnetic stirring and nitrogen atmosphere 1 hour before raising the temperature. Lastly, 500 µL of MilliQ water was added to the reaction batch according to Hemery et al.[18] and the temperature was increased under reflux up to 220°C. After cooling, the particles were magnetically separated and washed in HNO_3 (10%) to remove excess iron salts and confer to the NP surface a stabilizing positive charge; then twice with ethanol and acetone, before

dispersing the final product in MilliQ water. The surface of IONFs was modified by grafting citric acid, to improve water-solubility, and oleic acid, to obtain a stable ferrofluid in aprotic polar solvents. In brief, tri-sodium citric acid salts were dissolved in the aqueous ferrofluid, in a mole ratio $n_{C_6H_5Na_3O_7}/n_{NP}^{Fe}$ equal to 0.13. The solution was heated to boil for 40 minutes and after cooling the product was washed thrice with acetone and twice with ethyl ether, before being dispersed in MilliQ water. Ammonia solution was added equimolarly to liquid oleic acid 10 = n_{OA}/n_{NP}^{Fe} and magnetically stirred, in order to obtain a white thick mixture. At this point, also the IONF aqueous suspension was added and the solution was let stir for 10 minutes at room temperature. Afterwards, the temperature was raised to 50°C for 30 min and the product was separated from the solvent by magnetic separation. It was also washed three times with 60 mL of methanol and, after the last washing step, methanol was removed and a shiny precipitate was obtained; the final product was dispersed in tetrahydrofuran anhydrous. The oleate-coated IONFs were used for the microfluidic synthesis of magnetic micelles, while citrated NFs were used as a control in all experiments.

2.3 Microfluidic high throughput synthesis and scaling up of magnetomicelles

Magnetomicelles were formed by nanoprecipitation: two solutions of PS-b-PAA (Mn = 41,000-b-4200, 1.8 g/L) and oleic acid coated IONFs (0.2 g/L) were mixed in a ratio of 4:1 v/v to prepare a stock solution that was ultrasonicated for some minutes before use. Three ECP2000 Analytical HPLC pumps (ECOM spol. s r.o., Czech Republic) were connected to a stainless-steel cross junction: one central inlet was connected to the 150 μm PEEK tube and it was used for injecting the solution of block copolymer and NFs in THF; two symmetrical inlets were used to pump MilliQ water. The outlet consisted of a flow focusing system, with water surrounding a THF focalized stream. Water and THF were pumped into the system in a 7:1 v/v ratio (α) at variable total flow rates (Q_{tot} = 0.4 – 22.8 mL/min). All syntheses were conducted in triplicate, to assess reproducibility. After synthesis, a mass of MilliQ water equal to half of the total mass of the fluid mixture was rapidly added to quench the growth of micelles and preserve the obtained conformation. The resulting solution was collected in a pear-shaped flask to eliminate THF through rotary evaporation (BUCHI rotavapor R-210, connected to a BUCHI vacuum pump V-700 and employing a BUCHI heating bath B-491). The micellar water suspension was filtered with a 0.45 μm Minisart® filter unit (Sartorius, Gottingen, Germany), it was let to precipitate on a

permanent magnet and the pellet was collected and washed thrice with MilliQ water and subsequently stored at 4°C.

2.4 Nanostructure's characterizations

The morphology of the NPs was imaged using a JEOL-1011 transmission electron microscope operating at 100 kV. Size distributions were determined using the opensource ImageJ software, manually measuring 300 NPs on at least three different images. The resulting histograms were modelled by a log-normal law using Igor Pro 7 software to determine the mean physical diameter (d_{TEM}) and the polydispersity (σ_{TEM}) of each sample. The total iron concentrations of NPs suspensions were measured by atomic absorption spectroscopy (AAS, PinAAcle 500, PerkinElmer) by degrading the samples in concentrated HCl (37%) before a dilution in HNO_3 (2%). UV−Vis−NIR spectra (400−1100 nm) were recorded at room temperature in a 1 cm quartz cuvette using an Avantes spectrophotometric setup composed of an AvaLight-DHc lamp connected by optical fibers to a StarLine AvaSpec UV/Vis detector and to a NIRLine AvaSpec-NIR256−1.7 NIR detector. Aqueous suspensions were measured by VSM analysis in a static magnetic field comprised between - 1 T and 1 T at 300 K. Infrared PT experiments were carried out using a 0.5 mL Eppendorf® containing 50 µL of the NP suspensions excited for 300 s by a NIR laser (1064 nm, 0.28 W/cm^2) coupled to an optical fibre from Laser Components SAS (temperature increase is measured by an infrared camera FLIR SC7000).

3. Spheroids

3.1 Spheroids formation

U-87 MG human glioblastoma cells were selected for cancer cell line model, and purchased from ATCC®. They were cultured in Dulbecco's Modified Eagle Medium (DMEM, Gibco®), supplemented with 1% penicillin-streptomycin (PS, Gibco®) and with 10% fetal bovine serum (FBS, Gibco®), within a 37°C humidified incubator with 5% CO_2. Flasks of U87 cells were incubated at 37°C and 5% CO_2 overnight, with NP-doped complete culture medium (DMEM containing PS and FBS). IONF NPs were incubated at a dose of 0.05 mM while IONF@PS-b-PAA NPs were incubated at a dose of 0.5 mM. After the incubation, the cells were let 1 extra hour in the incubator at 37°C to allow the complete internalization of the nanoparticles adsorbed at the external membrane of cells; successively, cells were rinsed with complete medium, detached and

counted. Cellular pellet was formed by centrifugation and subsequently dispersed in an appropriate amount of fresh culture medium. The resulting volume was then separated in 0.5 mL Eppendorf® (each containing 200 000 cells), centrifuged at 180xg and incubated at 37°C to allow cell-to-cell adhesion and the formation of the spheroids.

3.2 Spheroids characterization

3.2.1 Vibrating Sample Magnetometry (VSM): Spheroids were fixed at different maturation days. They were washed with PBS and placed in a paraformaldehyde solution (PFA, 4% in PBS) for 2 hours at room temperature. Afterwards, the fixative solution was removed, spheroids were washed twice with PBS and stored at 4°C before characterizations. Magnetometry analyses was conducted on 10 spheroids samples (n=10) for each maturation time using a Quantum Design PPMS® at 300 K between 0 T and 2 T, or between -0.15 T to 0.15 T.

3.2.2 Iron concentration determination: iron concentrations were obtained by induced-coupled plasma atomic emission spectroscopy (ICP-AES, iCAP 6500, Thermo) after degradation of 10 spheroids (n=10) for each maturation time in concentrated HNO_3 (68%) before a dilution in water (up to 2%).

3.2.3 Transmission Electron Microscopy: prior to their observation, spheroids (n=5) were fixed at different maturation days for inclusion. They were washed five times in cacodylate buffer (0.1 mol·L) for 10 minutes under orbiting agitation. They were contrasted with oolong tea extract (OTE, 0.2%) in cacodylate buffer (0.1 mol·L) and newly washed according to the previously described procedure. Samples were then post-fixed with a solution in cacodylate buffer (0.1 mol·L) of osmium tetroxide (OsO_4, 1%) and potassium ferrocyanide (KFC, 1.5%), on ice and sheltered from light. Samples were washed in ultrapure water and successively enrobed in agarose (4% in ultrapure water). Samples are then dehydrated with successive baths of ethanol (once at 50%, once at 70%, once at 95%, once at 100% and five times at 100% absolute ethanol, purchased from VWR) for 15 minutes on ice. Impregnation with epoxy resin (Epon) was obtained through subsequent baths under rotary agitation in absolute ethanol/resin mixtures (1:2 v/v for 1 hour, 1:3 v/v overnight and 1:4 for 1.5 hours), in pure resin (two baths of 3 hours and overnight) and in pure resin with benzyldimethylamine (BDMA) polymerization accelerator (two baths of 3 hours after degassing the samples under vacuum for 30 minutes). Then, a bed of resin with BDMA was poured in molds and polymerized at 60°C for an hour, before positioning the samples and covering them with resin

and storing them in the pre-heated stove at 60°C for polymerization (lasting 72 hours). Ultrathin sample slices of 100 nm were obtained with an UCT ultramicrotome (Leica). Sample cuts were collected and placed on carbon coated copper grids 200 mesh; then, contrast was reinforced after staining with a solution of uranyl acetate (2.5% in water, 15 minutes sheltered from light). The morphology of the internalized NPs in cells was imaged using alternatively a JEOL-1011 transmission electron microscope operating at 100 kV, equipped with a charge-coupling derived camera (Orius) or a JEM-2100 transmission electron microscope (JEOL) operating at 80 kV with a LaB6 filament and equipped with a 2k × 2k Veleta charge-coupling camera (Olympus Soft Imaging Solutions).

4. Determination of degradation % using VSM in the spheroids

First, aqueous suspensions of IONFs and IONFs@PS-b-PAA were measured by VSM analysis in a static magnetic field comprised between - 1 T and 1 T at 300 K, to retrieve the value of saturation magnetization (M_S) with $M_S = \frac{M_{MAX}}{m_{NPs}}$. M_{MAX} is the maximum saturation of the IONFs after reaching magnetic saturation (expressed in emu) and m_{NPs} is the mass of IONFs in the suspension, obtained from $m_{NPs} = \frac{V_{tot} \cdot \phi \cdot \rho_{\gamma\text{-}Fe_3O_4}}{100}$ where V_{tot} is the total volume of the suspension, ϕ is the volume fraction of IONFs in the suspension and ρ is the density of magnetite (ρ = 5.2 g·cm^{-3}). The average mass of magnetic NPs per spheroid derived from VSM ($m_{Day,i}$) for each day i (i = 1, 3, 7 and 14) was next calculated. The percentage of degradation of the NPs is calculated then by $(\%) = \frac{m_{Day,i} - m_{Day,i,ICP}}{m_{Day,i,ICP}} \times 100$ where $m_{Day,i,ICP}$ corresponds to the average mass of total iron *per* spheroid deduced by ICP-AES analysis for each maturation day i.

5. Magnetic resonance imaging (MRI) experiments

To investigate the effects of degradation on the MRI signal of the IONFs and IONFs@PS-b-PAA in spheroids, their T_2 relaxation time constants were measured on a 3 T MRI scanner (Siemens Magnetom Trio) using a 32-channel head coil. Samples contained spheroids treated with IONFs or with IONFs@PS-b-PAA. For each type, 4 samples (n=4) were prepared with different spheroid maturation days (1, 3, 7, and 10 days). To ensure careful measurement of T_2 relaxation times, the samples were submerged into a gel prepared with HEC and doped with Cu_2SO_4 to ensure the MRI signal of the environment around the spheroids were at a reasonable level, similar to human tissue

signal. For measuring T_2, a single-echo spin echo sequence was utilized. T_2-weighted images were acquired at 16 different echo times (TE) ranging between 8.5-1000 ms, with TR = 2000 ms. A field-of-view (FOV) of 12x12 cm^2 with 4 mm slice thickness was imaged, using a 128x102 acquisition matrix. Images were analyzed using an in-house MATLAB (Mathworks) script. A fixed size region of interest (ROI) was placed over the image region corresponding to each vial. The T_2 value for each sample at each pixel in the ROI was determined using the following monoexponential decay equation: $S=S_0e^{-TE/T_2}$

6. X-ray absorption measurements (XAS)

The X-ray data were acquired at the X-Treme beamline (Swiss Light Source, Paul Scherrer Institut). X-ray absorption measurements were performed on a collection of three spheroids (n=3) deposited on Si wafers for each maturation time. XAS at the Fe $L_{2,3}$ edges (700 – 730 eV) were collected at 300 K using the total electron yield mode of detection. The spectra were normalized by the edge jump at the maximum of the L_3 after background subtraction.

3. Results and Discussion

3.1 Encapsulation of IONFs in the micelles decreases their degradation as shown from VSM

Figures 1a and 1b show respectively, TEM images of the magnetite IONFs before and after encapsulation in the polymeric micelles. As displayed from the size histograms (insets in Figure 1a and b) fitted by a log-normal law, the IONFs have a diameter of 18.1 nm with a polydispersity of 0.19, as calculated from the size distribution histogram while the magnetic micelles are 51.8 nm in size with a polydispersity of 0.22. The IONFs were synthesized through the polyol process and the magnetic micelles were produced by self-assembly of the IONFs and the BCP using a high throughput microfluidic method, as described recently.[39] The magnetization curves for the colloidal aqueous suspensions of IONFs and magnetomicelles are shown in Figure S1. The citrated IONFs exhibited a saturation magnetization (M_S) of 79 emu·g_{NPs}^{-1}, consistent with previously reported values for magnetite IONFs.[17] However, the magnetomicelles showed a lower M_S value of 61 emu·g_{NPs}^{-1}, attributed to the presence of the polymeric material, as reported for iron oxides embedded in some matrices.[40, 41]

To investigate the impact of cancer cells processing on both types of nanostructures, a spheroid-forming human glioblastoma cell line (U87) was used as a cancer model. Cancer cells were incubated with both types of nanostructures to allow for their uptake by the cells at a biocompatible concentration and a final concentration (see materials and methods).[39] Due to their excellent stability, the micelles penetrate cells less readily compared to non-encapsulated bare IONFs, justifying a higher dose incubation for the micelles to achieve the same amount of cellular magnetism post-internalization. Following this, spheroids containing approximately 200,000 cells were formed and allowed to mature for up to 13 days at 37°C. The spheroids were fixed at different maturation days (1, 3, 7, 10, and 13 days, Figure S2). After internalization of the NPs in the cancer cells and the formation of the spheroids, we followed and quantified their

degradation in the cancer spheroids with days at the nanoscale using their magnetic fingerprints by vibrating sample magnotmetry (VSM).

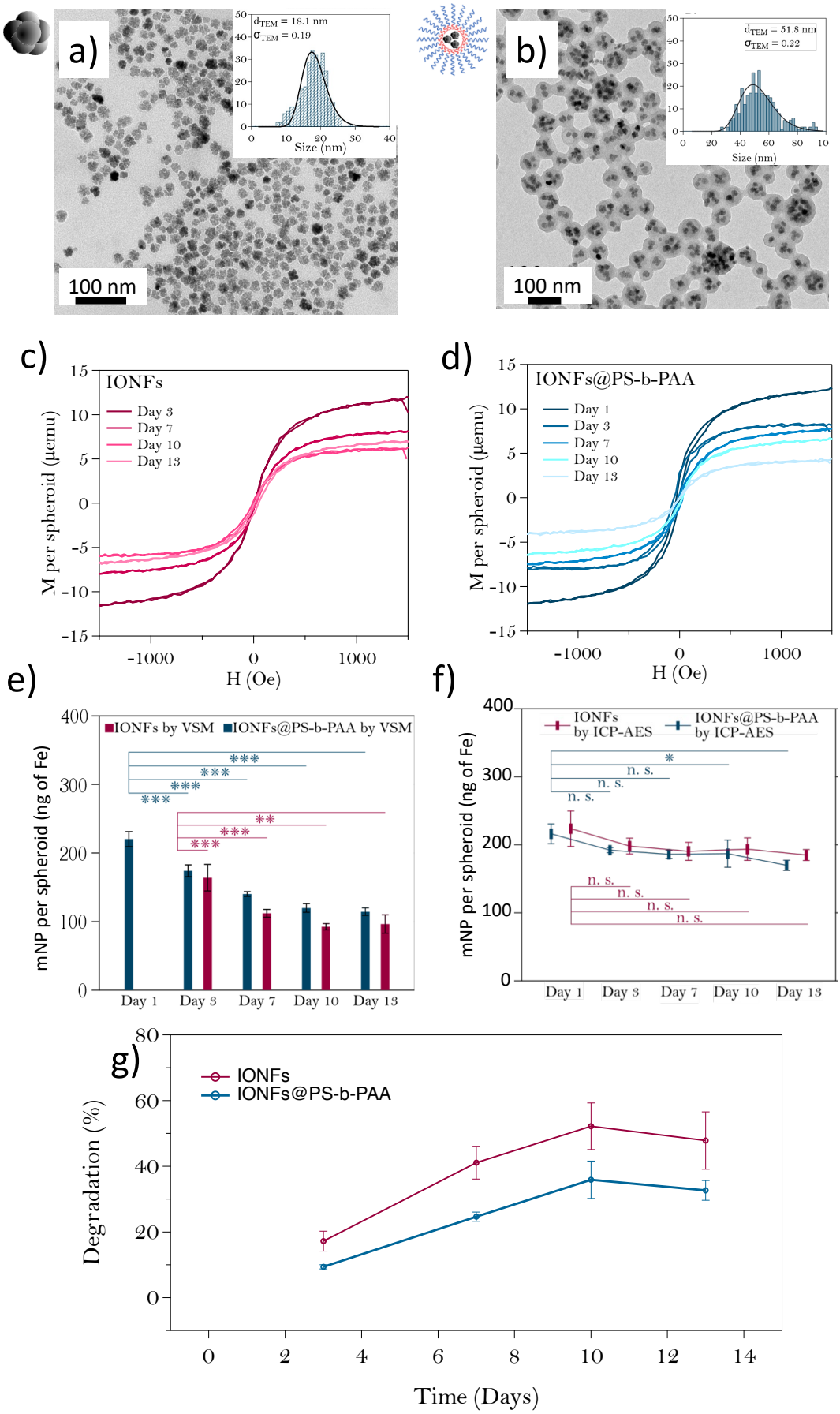
a)
100 nm
d_{TEM} = 18.1 nm
σ_{TEM} = 0.19
Size (nm)
b)
100 nm
d_{TEM} = 51.8 nm
σ_{TEM} = 0.22
Size (nm)
c)
IONFs
Day 3
Day 7
Day 10
Day 13
M per spheroid (μemu)
H (Oe)
d)
IONFs@PS-b-PAA
Day 1
Day 3
Day 7
Day 10
Day 13
M per spheroid (μemu)
H (Oe)
e)
IONFs by VSM
IONFs@PS-b-PAA by VSM
mNP per spheroid (ng of Fe)
Day 1
Day 3
Day 7
Day 10
Day 13
f)
IONFs by ICP-AES
IONFs@PS-b-PAA by ICP-AES
n. s.
mNP per spheroid (ng of Fe)
Day 1
Day 3
Day 7
Day 10
Day 13
g)
IONFs
IONFs@PS-b-PAA
Degradation (%)
Time (Days)

Figure 1. TEM image and their size distribution histogram fitted by a log-normal law for IONFs (a) and IONFs@PS-b-PAA magnetomicelles (b). Magnetization per spheroid measured after internalization in U87 cancer cells and maturation of a spheroid model (n=10) for 1, 3, 7, 10, and 13 days for IONFs (c) and IONFs@PS-b-PAA (d); e) Residual magnetic iron per spheroid expressed in ng measured by VSM for each maturation day (n=10) for both IONFs and IONFs@PS-b-PAA. Black bars stand for standard deviations. A two-tailed Student's t-test was used to assess the significance of residual magnetic iron for both samples on the same day (black trait and stars) and for same IONFs after 3, 7, 10, or 13 days of maturation (burgundy trait and stars for IONFs, blue trait and stars for IONFs@PS-b-PAA. 0.05>p-value>0.01 (*), 0.01>p-value>0.001 (**), p-value<0.001 (***); f) Total iron per spheroid (expressed in ng, n=10), measured by ICP-AES. Coloured bars stand for standard deviations. A two-tailed Student's t-test was used to assess the significance of residual magnetic iron for one same IONFs after 3, 7, 10, or 13 days of maturation. 0.05>p-value>0.01 (*), 0.01>p-value>0.001 (**), p-value<0.001 (***); g) Percentage of NPs degradation deduced from VSM measurements for IONFs and IONFs@PS-b-PAA.

As shown from Figure 1c and 1d, over time the magnetization of IONFs and IONFs@PS-b-PAA decreased progressively over maturation times indicating degradation of the iron oxide core. The average mass of IONFs per spheroid was then calculated from the VSM meaurements. The results showed that the mass of magnetic material per spheroid for both IONFs and magnetomicelles decreased with spheroid maturation time. Statistical analysis revealed significant differences in the mass of magnetic material between day one and other maturation days for most conditions. Such differences decreased with maturation time, becoming non-significant at day 3, and remaining non-significant at days 7, 10, and 13. ICP-AES measurements were performed to determine the average total iron concentration within single spheroids. Total iron per spheroid was perfectly similar for spheroids incubated with IONFs or with magnetomicelles. Besides, these values remained relatively stable over the whole maturation period, with yet a decreasing tendency in the amount of total iron per spheroid over the maturation period. To assess whether the decrease in total iron was due to cellular loss, the two-tailed Student's t-test was performed on sets of total iron values obtained for single spheroids at maturation day one against all other maturation days. Except for the spheroids with magnetomicelles at maturation day 13, which showed a significant difference, all other conditions did not exhibit significant differences, indicating minimal cellular loss. The percentage of degradation was calculated by considering the mass of magnetic material extracted from VSM and the average value of iron obtained by ICP-AES as detailed in the materials and methods. Results (Figure 1g) showed a general increase in the degradation percentage with maturation time for IONFs and magnetic micelles. However the degradation of

IONFs was faster than that of magnetic micelles reaching at day 13 a value of 48 (±9)% for IONFs and 33 (±3)% for IONFs@PS-b-PAA. These results suggest that the polymeric micelles can provide a protective behavior after internalization in U87 cells.

3.2 Photothermal function of IONFs lasted longer when encapsulated in the micelles

The UV-Vis-NIR extinction spectra of IONFs and the magnetomicelles are shown in Figure S3. Both spectra show a U-shaped absorption and an increase above 700 nm, characteristic of magnetite and its intervalence charge transfer band. However, the spectrum of the magnetomicelles displayed a slight decrease in the absorbance compared to the non-encapsulated IONFs which was attributed to the presence of the polymeric shell, with no significant impact on the heating efficacity of the encapsulated IONFs when irradiated in the NIR, as it was demonstrated in a previous work.[39] In order to assess the effect of intracellular degradation of nanomaterials on photothermal activity, we implemented a measurement protocol on spheroids under irradiation with an 808 nm laser at a power density of 1 W/cm². Under these conditions, the temperature elevation at single spheroid level is not detectable compared to nonspecific heating. Consequently, we systematically gathered 24 spheroids in a 0.5 mL Eppendorf tube containing 25 µL of culture medium (typical photograph of those multiple spheroids can be observed in Figures 2a and 2b). Figures 2a and 2b also depict the heating in an image captured by infra-red camera for 24 control spheroids (nonspecific heating) and for 24 spheroids composed of cells that have internalized magnetic micelles. Figures 2c and 2d display representative images of heating for the two types of nanomaterials, particularly at different stages of spheroid maturation, namely days 0, 1, 4, and 9. Each measurement was conducted on 4 independent samples, each containing 24 spheroids, for every time point, totaling 100 spheroids per data point (days 0,1,4,9, and 13), and thus approximately 500 spheroids in total. Figure S4 shows the temperature elevation curves for each sample, and Figures 2e-2g respectively show the average plateau temperatures achieved after 10 minutes of laser exposure, the equivalent temperature elevation, and the temperature elevation excluding the contribution of nonspecific heating. This clearly identifies a protection provided by the micelles against degradation, as quantified in Figure 2h, resulting in a longer-lasting photothermal potential for them.

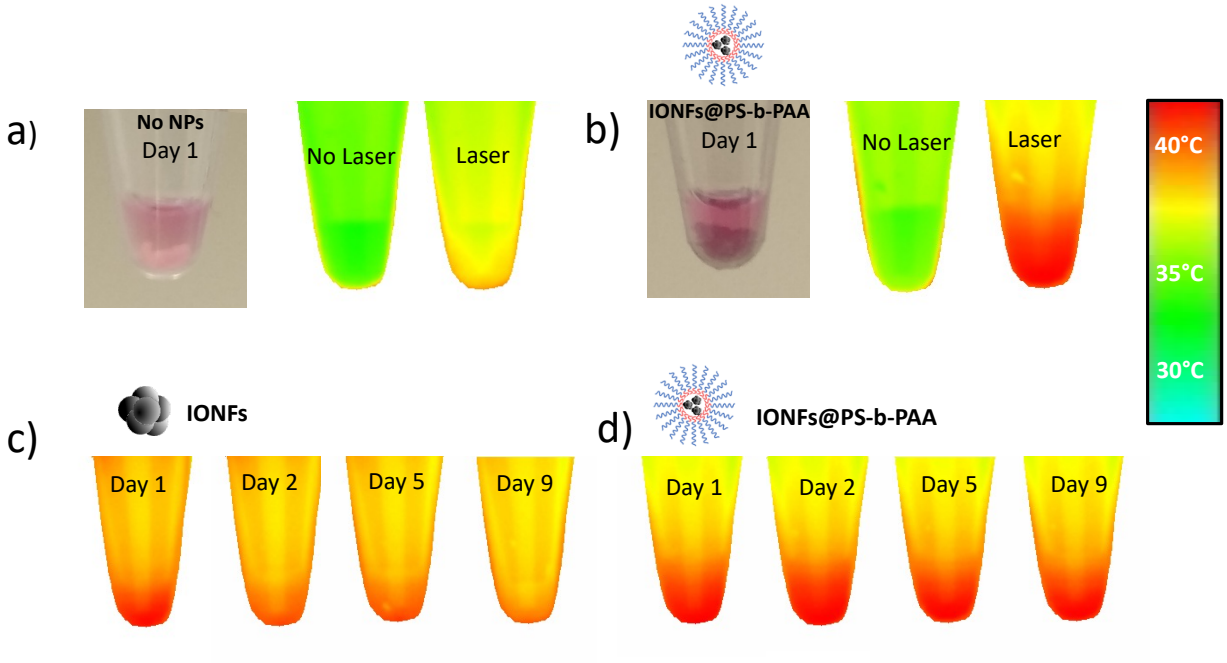
a)
No NPs
Day 1
No Laser
Laser
b)
IONFs@PS-b-PAA
Day 1
No Laser
Laser
40°C
35°C
30°C
c)
IONFs
Day 1
Day 2
Day 5
Day 9
d)
IONFs@PS-b-PAA
Day 1
Day 2
Day 5
Day 9

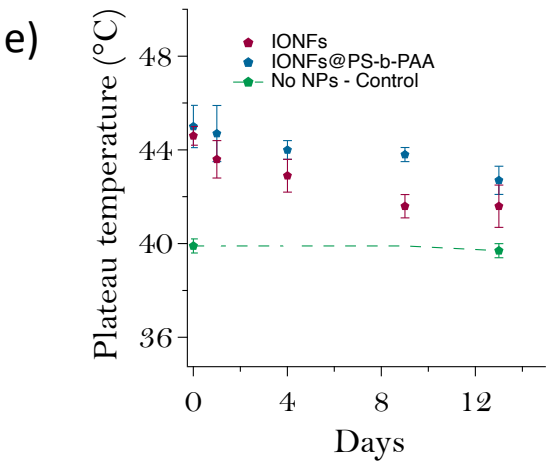
e)
IONFs
IONFs@PS-b-PAA
No NPs - Control
Plateau temperature (°C)
48
44
40
36
0
4
8
12
Days

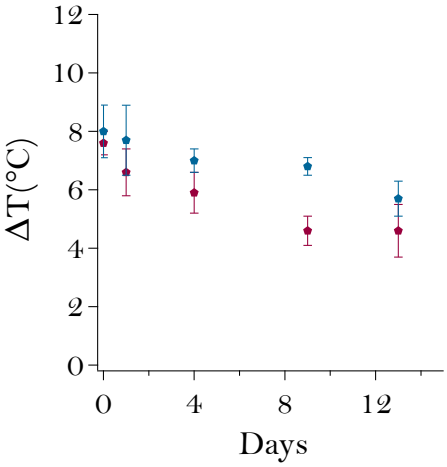
f)
ΔT(°C)
12
10
8
6
4
2
0
0
4
8
12
Days

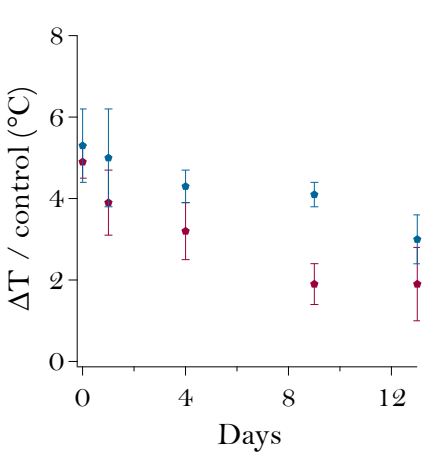
g)
ΔT / control (°C)
8
6
4
2
0
0
4
8
12
Days

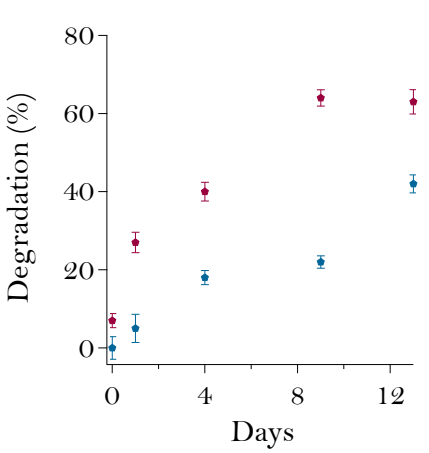
h)
Degradation (%)
80
60
40
20
0
0
4
8
12
Days

Figure 2. After the formation of the spheroids, they are individually collected in 0.5 mL Eppendorf tubes, with a quantity of 24 spheroids per tube in 25 µL. For the condition shown in (a), the spheroids are control spheroids, which have not been in contact with nanoparticles. They appear relatively white and exhibit minimal heating under an IR laser at 1W/cm² (images captured by the IR camera shown on the right before and after laser application - over a duration of 10 minutes). Panel (b) depicts the same data, but for spheroids fabricated from cells that have internalized magnetic micelles. Heating is more significant, reaching about 46°C over 10 min of laser exposure. The panels (c) and (d) depict once again the heating of n=24 spheroids in a 0.5 mL Eppendorf tube filled with 25 µL, but this time not only on day 0 (as in panels a and b), but also on days 1, 4, and 9. In panel (c), the spheroids were formed from cells that internalized the nanoflowers, while in panel (d), it was cells that internalized the magnetic micelles. For each time point, measurements were performed on 4 sets of n=24 independent spheroids. The average plateau temperature reached is shown in panel (e), the temperature increase is shown in panel (f), and normalized to the control in panel (g). Finally, the percentage of degradation is calculated and shown in panel (h).

2.3 Nanoscale observations by electron microscopy evidence that cancer cells can overcome the polymeric PS core barrier and induce slight biodegradation of IONFs

We next tracked at the nanoscale the morphological features of IONFs including in the micelles when processed by the cancer cells. For this, slices of the fixed spheroids were imaged at different days using TEM. Representative microtomy images of the U87 spheroids formed with cells containing either IONFs or magnetomicelles are shown in Figure 3. For spheroids fixed at day 1 of maturation, no significant changes were observed between the size distribution of the IONFs in suspension and in the cells. In addition, they were initially found in membrane-enclosed compartments of the cytosol, mainly identifiable as early endosomes (Figure 3a). Higher magnification micrographs of the same IONFs on day 1 (Figure 3b) also reveal IONFs enclosed in larger vesicle, resembling double-layered autolysosome, associated with autophagy-related acidic degradation pathways.[42] This result aligns with cancer cell enhanced metabolism and autophagy, to escape apoptotic programmed cell death and promote cell survival in case of metabolic stress. Autophagy is also related to cancer cells' ability to develop resistance to external stressors, including chemotherapeutic drugs and nanoparticles.

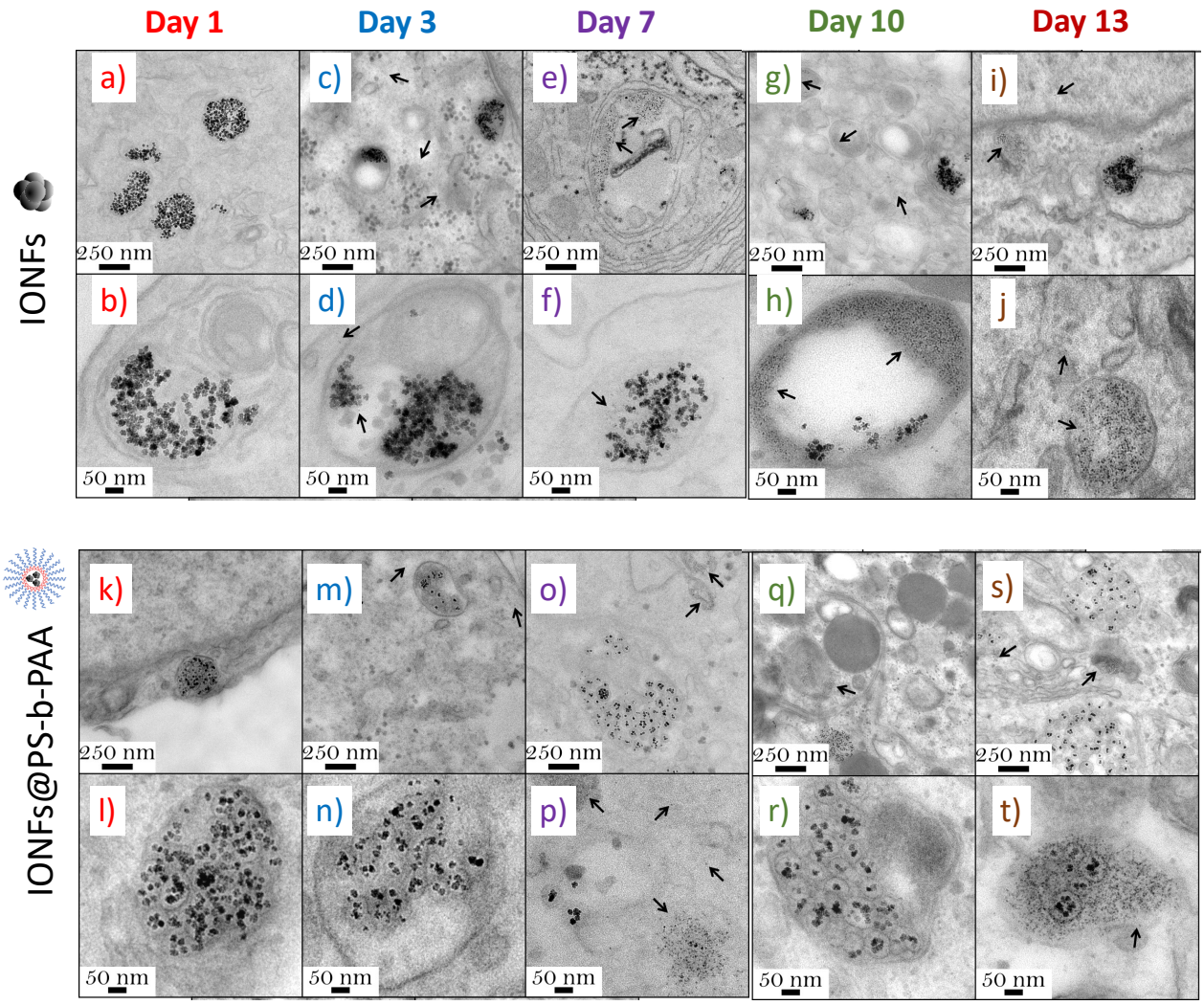

Figure 3. Representative TEM micrographs of IONFs (a-j) and IONFs@PS-b-PAA (k-t) NPs after internalization in U87 cells for different days: 1-day-long (a, b, k, l), 3-days-long (c, d, m, n), 7-days-long (e, f, o, p), 10-days-long (g, h, q, r) and 13-days-long (i, j, s, t) maturation into spheroid models. Black arrows indicate ferritin-enriched areas. More images are provided in the supplementary material Figures S5 and S6.

Micrographs on day 3 of spheroid maturation showed the co-localization of IONFs in grey-contrasted organelles, probably derived from the fusion of endosomes with lysosomes (Figures 3c and d). Iron-loaded ferritin, indicated by black arrows, was also observed in these structures, suggesting that the endocytic compartments underwent acidification, leading to the appearance of

iron-loaded ferritin. From maturation days 7, 10, and 13 (Figures 3e-j) low-contrast 4-7 nm spheres consistent with iron-charged ferritin were found within multi-membrane amphisomes or auto- and endolysosomes. In contrast, very few intact IONFs were detected on the grid in the same vesicles. However, some endosomes containing only intact IONFs were also present, confirming that degradation occurred sporadically at the level of single vesicles.

Regarding the spheroids incubated with magnetomicelles, the nanostructures were mainly localized in early endosomes (Figures 3k and l) or autophagosomes (displaying portions of double-layered membranes, as shown in Figures 3m-n up to three days after incubation with cells. Notably, not all IONFs appeared to be encircled by the polymeric shell; some seemed to have freed in the endosomal lumen. Starting from the third day of spheroid maturation, the presence of iron-loaded ferritin (Figure 3n) indicated the degradation of IONFs, likely through the same acidic pathway observed for IONFs. The ferritin-like spheres were found in both membrane-enclosed dark grey compartments and in the cytosol at maturation day 7 (Figures 3o-p), suggesting lysosomal engagement. This was further confirmed by micrographs obtained at maturation day 10 (Figures 3q-r), showing autophagolysosomes and endolysosomes. Even after 13 days of magnetomicelles internalization in U87 cells, ferritin-enriched areas were still identifiable in dark-grey endosomes and free in the cytoplasm, next to intact IONF@PS-b-PAA NPs (Figures 3s-t). Interestingly, one micrograph (Figure 3t) showed the coexistence of iron-loaded ferritin, intact magnetomicelles, and empty non-denatured polymeric "ghost" shells (where ferritin appeared to stick onto the polymeric surface). This observation confirmed the escape of IONFs through degradation from the still intact polymeric shell, rather than the disruption or degradation of the polymer itself. The size of the intact shells did not show any significant change in the size compared to the initial suspension of magnetic micelles.

2.4 MRI and XAS investigations confirmed the biodegradation of IONFs and the formation of ferritin

IONFs were recently described as excellent T_2 contrast agents for MRI.[39] Here, we used their T_2-weighted MRI after internalization in the spheroids to monitor their degradation with time. Figure S7 illustrates an example T_2-weighted MRI image, depicting eight spheroid samples within the gel environment. Figure 4a shows how T_2 changes for IONFs and magnetomicelles on days 1, 3, 7, and 10 with maturation time. Lower T_2 values indicate better MRI contrast performance. Notably, the T_2 values for both IONFs and magnetomicelles increase with time, suggesting a gradual loss

of MRI contrast performance due to degradation. Statistical analysis via two-tailed Student's t-test revealed significant differences in T_2 values between day 1 and day 10 for both IONFs and magnetomicelles. This behavior can be attributed to degradation-induced reduction in the effective concentration of magnetic nanoparticles within the spheroids for both cases.[43]

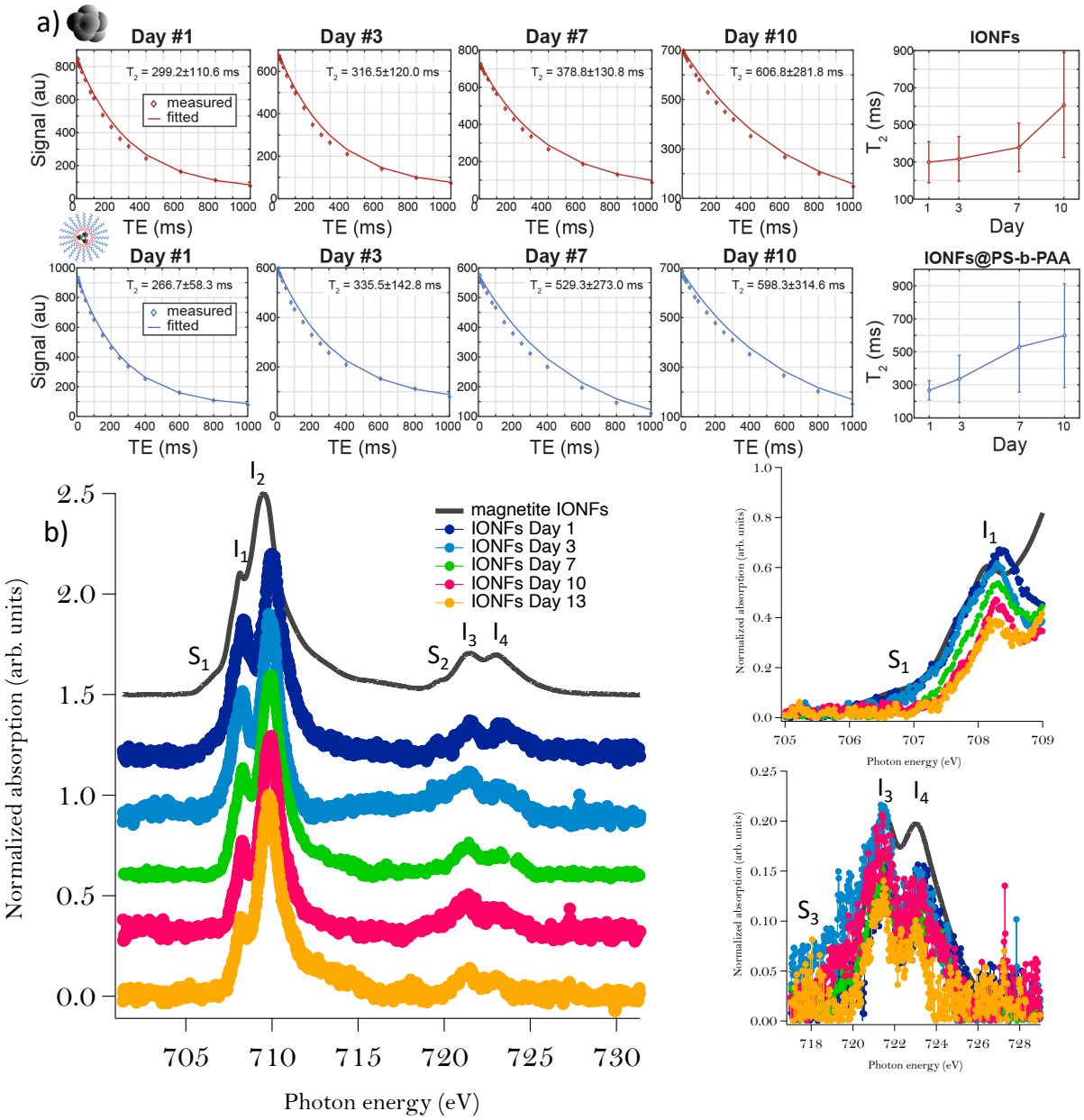

Figure 4. a) MRI T_2 relaxation times for different maturation days for IONFs and IONFs@PS-b-PAA and as a function of days with increased T_2 indicating degradation of the nanoparticles (n=4). Error bars denote standard deviations; b) XAS at the Fe $L_{2,3}$ edges performed on the IONFs spheroids (n=3) for maturation times of 1, 3, 7, 10 and 13 days. The results can be compared with

the XAS acquired on the magnetite reference nanoparticles as synthesized (before internalization). The insets show the normalized XAS data for comparison in the L_3 edge (top panel) and L_2 edge (bottom panel).

Additionally, Figure 4a shows that both IONFs and magnetomicelles display comparable T_2 values on day 10. Taken together, TEM images and MRI demonstrate that cancer cells can bioprocess the magnetic nanoparticles leading to their degradation which correlates well with the decrease in their magnetic properties observed by VSM and photothermal measurements. These results also demonstrate that, despite their encapsulation inside a polymeric barrier of PS with high glass transition, chemical species in the cancer cell can still access to the magnetic nanoparticles inducing their degradation. Indeed, Vyhnalkova *et al*.[38] have shown that small species are capable to diffuse in empty PS-b-PAA polymeric micelles leading to a decrease in the glass transition temperature of the BCP, an increase in the mobility of PS chains, enabling access of species to the core of the micelle. In addition an acidic pH as encountered in the endosomal compartments of cancer cells may affect the conformational behaviour of the hydrophilic PAA corona or even lead to its degradation.[27, 44] Taking together these elements we may draw the following hypothesis in the cancer cells where the harsh physicochemical conditions (pH, ROS, etc) and high metabolism can lead to the formation of different species capable to diffuse into the core of the micelles leading to the degradation of IONFs through their dissolution into iron species.

To further investigate the chemical and structural changes in the IONFs during their degradation, we examined the X-ray absorption spectroscopy (XAS) at the Fe $L_{2,3}$ edges for various maturation time points, as shown in Figure 4b. Before internalization in spheroids the citrated magnetite IONFs used as a reference, presented a typical $L_{2,3}$ edges resonance spectrum with a prominent feature at 709.5 eV (I_2) and a lower intensity peak at 708 eV (I_1) at the L_3 edge, and two smaller features at 721.5 eV (I_3) and 723 eV (I_4) for the L_2 edge.[45-47] In addition, small shoulders at lower energies ~706.3 eV and ~719 eV of the L_3 and L_2 edges respectively revealed the clear presence of octahedral coordinated Fe^{2+}. Qualitatively, the contributions of octahedral Fe^{2+} is not as strong as expected for a stoichiometric bulk magnetite revealing that the magnetite particles are slightly oxidized.[48, 49] Right after internalization (day 1) and compared with the IONFs in water, a more pronounced splitting of the L_3 edge and increased prominence of I1 was observed. This was accompanied with a higher ratio in the intensity of I_3/I_4. Taking into accounts that no degradation was spotted at day 1 by VSM, PT and TEM measurements, this observation may be explained by the presence of native Fe^{2+} pool in the spheroids which contributes in addition to magnetite IONFs

to the final XAS signal. Furthermore, with spheroids maturation days we noticed additional evolutions of the isotropic signal contributions. From day 1 to day 13, this peak at the L_2 edge, experienced a clear decay with the maturation time of the spheroids. Simultaneously, the I_3/I_4 ratio gradually increased from day 1 to day 3, while S1 and S2 contributions decreased, disappearing by day 13. These results indicate a process of oxidation of the ferrous species which can occur through transformation into another phase of IONFs. The shape of the XAS spectra indicates that as the spheroids mature, they contain Fe atoms in an environment characteristic of ferrihydrite.[50, 51] These results agree well with the images obtained at the nanoscale by TEM showing the degradation of IONFs and formation of ferritin. Precise crystalline phase of the nanoparticles during maturation may be sensitive to XAS features due to the possible mixing of different iron oxide phases, but this is beyond the scope of our current study. Nevertheless, we can confidently conclude that IONFs evolve into a more oxidized ferrihydrite phase with maturation time.

4. Conclusions

In this paper we investigated the bioprocessing of IONFs and magnetic micelles made by self-assembly of IONFs and PS-b-PAA block copolymer in a U-87 glioblastoma cancer spheroids. Using different characterization tools, we monitored the biotransformation of the assembled structures and non-encapsulated IONFs at different times and length scales. We showed that while the polymeric barrier around the magnetic nanoparticles is kept intact it can be overcome by the harsh physicochemical conditions of the cancer cells inducing partially the degradation of the magnetic nanoparticles in the core of the micelles and the formation of ferritin. Yet, degradation is less pronounced for the magnetomicelles than for the non-encapsulated IONFs. On the therapeutic side, this protection translates into a longer-lasting photothothermal performance of the magnetomicelles. These results therefore underly the potential of micelles as nanocarriers and protection agents for inorganic nanoparticles and may open new perspectives for the development of innovative therapies in the field of nanomedecine such as in drug delivery or tissue engineering.

ASSOCIATED CONTENT

Supporting Information.

Magnetization measurements, images of the spheroids, absorption spectra, temperature elevation curves, representative microtomy images and T_2-weighted MRI image (file type, i.e., PDF)

AUTHOR INFORMATION

Corresponding Author

Ali Abou-Hassan ali.abou_hassan@sorbonne-universite.fr

Author contributions

The manuscript was written through contributions of all authors. All authors have given approval to the final version of the manuscript.

Acknowledgements:

E. B. and A. A.-H acknowledge the support of the French Agence Nationale de la Recherche (ANR), under grant ANR-18-CE09-0004 (project MicroNanoCell). A. A.-H. and C. W. acknowledge the support of the French Agence Nationale de la Recherche (ANR), under grant ANR-19-CE09-0029 (project SuperMagStemCells). We acknowledge Alexis Canette from the IBPS electron microscopy core facility and the support of « Région Île-de-France », Sorbonne-Université and CNRS for his assistance with sample preparation using the Pelco Biowave instrument. N.D acknowledges the Swiss National Foundation for the support under the Ambizione grant PZ00P2_193293. A. A.-H. acknowledges Ana Hortelão for fruitful discussions.

References

(1) Shieh, D.-B.; Cheng, F.-Y.; Su, C.-H.; Yeh, C.-S.; Wu, M.-T.; Wu, Y.-N.; Tsai, C.-Y.; Wu, C.-L.; Chen, D.-H.; Chou, C.-H. Aqueous dispersions of magnetite nanoparticles with NH3+ surfaces for magnetic manipulations of biomolecules and MRI contrast agents. *Biomaterials* **2005**, *26* (34), 7183-7191. DOI: https://doi.org/10.1016/j.biomaterials.2005.05.020

(2) Rigoni, C.; Fresnais, J.; Talbot, D.; Massart, R.; Perzynski, R.; Bacri, J. C.; Abou-Hassan, A. Magnetic Field-Driven Deformation, Attraction, and Coalescence of Nonmagnetic Aqueous Droplets in an Oil-Based Ferrofluid. *Langmuir* **2020**, *36* (18), 5048-5057. DOI: 10.1021/acs.langmuir.0c00060

(3) Di Corato, R.; Quarta, A.; Piacenza, P.; Ragusa, A.; Figuerola, A.; Buonsanti, R.; Cingolani, R.; Manna, L.; Pellegrino, T. Water solubilization of hydrophobic nanocrystals by means of poly(maleic anhydride-alt-1-octadecene). *Journal of Materials Chemistry* **2008**, *18* (17), 1991-1996, 10.1039/B717801H. DOI: 10.1039/B717801H

(4) Filippi, M.; Garello, F.; Yasa, O.; Kasamkattil, J.; Scherberich, A.; Katzschmann, R. K. Engineered Magnetic Nanocomposites to Modulate Cellular Function. *Small* **2022**, *18* (9), 2104079. DOI: https://doi.org/10.1002/smll.202104079

(5) Van de Walle, A.; Figuerola, A.; Espinosa, A.; Abou-Hassan, A.; Estrader, M.; Wilhelm, C. Emergence of magnetic nanoparticles in photothermal and ferroptotic therapies. *Materials Horizons* **2023**, *10* (11), 4757-4775, 10.1039/D3MH00831B. DOI: 10.1039/D3MH00831B

(6) Espinosa, A.; Kolosnjaj-Tabi, J.; Abou-Hassan, A.; Plan Sangnier, A.; Curcio, A.; Silva, A. K. A.; Di Corato, R.; Neveu, S.; Pellegrino, T.; Liz-Marzán, L. M.; et al. Magnetic (Hyper)Thermia or Photothermia? Progressive Comparison of Iron Oxide and Gold Nanoparticles Heating in Water, in Cells, and In Vivo. *Advanced Functional Materials* **2018**, *28* (37), 1803660. DOI: https://doi.org/10.1002/adfm.201803660

(7) Gavilán, H.; Avugadda, S. K.; Fernández-Cabada, T.; Soni, N.; Cassani, M.; Mai, B. T.; Chantrell, R.; Pellegrino, T. Magnetic nanoparticles and clusters for magnetic hyperthermia: optimizing their heat performance and developing combinatorial therapies to tackle cancer. *Chemical Society Reviews* **2021**, *50*, 11614-11667. DOI: https://doi.org/10.1039/d1cs00427a

(8) Avugadda, S. K.; Wickramasinghe, S.; Niculaes, D.; Ju, M.; Lak, A.; Silvestri, N.; Nitti, S.; Roy, I.; Samia, A. C. S.; Pellegrino, T. Uncovering the Magnetic Particle Imaging and Magnetic Resonance Imaging Features of Iron Oxide Nanocube Clusters. *Nanomaterials* **2021**, *11* (1), 62.

(9) Cazares-Cortes, E.; Cabana, S.; Boitard, C.; Nehlig, E.; Griffete, N.; Fresnais, J.; Wilhelm, C.; Abou-Hassan, A.; Ménager, C. Recent insights in magnetic hyperthermia: From the "hot-spot" effect for local delivery to combined magneto-photo-thermia using magneto-plasmonic hybrids. *Advanced Drug Delivery Reviews* **2019**, *138*, 233-246. DOI: https://doi.org/10.1016/j.addr.2018.10.016

(10) Jain, T. K.; Reddy, M. K.; Morales, M. A.; Leslie-Pelecky, D. L.; Labhasetwar, V. Biodistribution, Clearance, and Biocompatibility of Iron Oxide Magnetic Nanoparticles in Rats. *Molecular Pharmaceutics* **2008**, *5* (2), 316-327. DOI: 10.1021/mp7001285

(11) Nemec, S.; Kralj, S.; Wilhelm, C.; Abou-Hassan, A.; Rols, M.-P.; Kolosnjaj-Tabi, J. Comparison of iron oxide nanoparticles in photothermia and magnetic hyperthermia: Effects of clustering and silica encapsulation on nanoparticles' heating yield. *Applied Sciences* **2020**, *10* (20), 7322.
(12) Cabana, S.; Curcio, A.; Michel, A.; Wilhelm, C.; Abou-Hassan, A. Iron oxide mediated photothermal therapy in the second biological window: A comparative study between magnetite/maghemite nanospheres and nanoflowers. *Nanomaterials* **2020**, *10* (8), 1548.
(13) Roca, A. G.; Lopez-Barbera, J. F.; Lafuente, A.; Özel, F.; Fantechi, E.; Muro-Cruces, J.; Hémadi, M.; Sepulveda, B.; Nogues, J. Iron oxide nanoparticles (Fe3O4, γ-Fe2O3 and FeO) as photothermal heat mediators in the first, second and third biological windows. *Physics Reports* **2023**, *1043*, 1-35. DOI: https://doi.org/10.1016/j.physrep.2023.10.003
(14) Bertuit, E.; Benassai, E.; Mériguet, G.; Greneche, J.-M.; Baptiste, B.; Neveu, S.; Wilhelm, C.; Abou-Hassan, A. Structure–Property–Function Relationships of Iron Oxide Multicore Nanoflowers in Magnetic Hyperthermia and Photothermia. *ACS Nano* **2022**, *16* (1), 271-284. DOI: 10.1021/acsnano.1c06212
(15) Bertuit, E.; Menguy, N.; Wilhelm, C.; Rollet, A.-L.; Abou-Hassan, A. Angular orientation between the cores of iron oxide nanoclusters controls their magneto–optical properties and magnetic heating functions. *Communications Chemistry* **2022**, *5* (1), 164. DOI: 10.1038/s42004-022-00787-0
(16) Gallo-Cordova, A.; Ovejero, J. G.; Pablo-Sainz-Ezquerra, A. M.; Cuya, J.; Jeyadevan, B.; Veintemillas-Verdaguer, S.; Tartaj, P.; del Puerto Morales, M. Unravelling an amine-regulated crystallization crossover to prove single/multicore effects on the biomedical and environmental catalytic activity of magnetic iron oxide colloids. *Journal of Colloid and Interface Science* **2022**, *608*, 1585-1597.
(17) Gavilán, H.; Sánchez, E. H.; Brollo, M. E. F.; Asín, L.; Moerner, K. K.; Frandsen, C.; Lázaro, F. J.; Serna, C. J.; Veintemillas-Verdaguer, S.; Morales, M. P.; et al. Formation Mechanism of Maghemite Nanoflowers Synthesized by a Polyol-Mediated Process. *ACS Omega* **2017**, *2* (10), 7172-7184. DOI: 10.1021/acsomega.7b00975
(18) Hemery, G.; Keyes, A. C.; Garaio, E.; Rodrigo, I.; Garcia, J. A.; Plazaola, F.; Garanger, E.; Sandre, O. Tuning Sizes, Morphologies, and Magnetic Properties of Monocore Versus Multicore Iron Oxide Nanoparticles through the Controlled Addition of Water in the Polyol Synthesis. *Inorganic Chemistry* **2017**, *56* (14), 8232-8243. DOI: 10.1021/acs.inorgchem.7b00956
(19) Roy, S.; Liu, Z.; Sun, X.; Gharib, M.; Yan, H.; Huang, Y.; Megahed, S.; Schnabel, M.; Zhu, D.; Feliu, N.; et al. Assembly and Degradation of Inorganic Nanoparticles in Biological Environments. *Bioconjugate Chemistry* **2019**, *30* (11), 2751-2762. DOI: 10.1021/acs.bioconjchem.9b00645
(20) Feliu, N.; Docter, D.; Heine, M.; del Pino, P.; Ashraf, S.; Kolosnjaj-Tabi, J.; Macchiarini, P.; Nielsen, P.; Alloyeau, D.; Gazeau, F.; et al. In vivo degeneration and the fate of inorganic nanoparticles. *Chemical Society Reviews* **2016**, *45* (9), 2440-2457, 10.1039/C5CS00699F. DOI: 10.1039/C5CS00699F

(21) Lu, H.; Stenzel, M. H. Multicellular Tumor Spheroids (MCTS) as a 3D In Vitro Evaluation Tool of Nanoparticles. *Small* **2018**, *14* (13), 1702858. DOI: https://doi.org/10.1002/smll.201702858
(22) Curcio, A.; de Walle, A. V.; Benassai, E.; Serrano, A.; Luciani, N.; Menguy, N.; Manshian, B. B.; Sargsian, A.; Soenen, S.; Espinosa, A. Massive intracellular remodeling of CuS nanomaterials produces nontoxic bioengineered structures with preserved photothermal potential. *ACS nano* **2021**, *15* (6), 9782-9795.
(23) Mazuel, F.; Espinosa, A.; Radtke, G.; Bugnet, M.; Neveu, S.; Lalatonne, Y.; Botton, G. A.; Abou-Hassan, A.; Wilhelm, C. Magneto-thermal metrics can mirror the long-term intracellular fate of magneto-plasmonic nanohybrids and reveal the remarkable shielding effect of gold. *Advanced Functional Materials* **2017**, *27* (9), 1605997.
(24) Espinosa, A.; Curcio, A.; Cabana, S.; Radtke, G.; Bugnet, M.; Kolosnjaj-Tabi, J.; Péchoux, C.; Alvarez-Lorenzo, C.; Botton, G. A.; Silva, A. K. A.; et al. Intracellular Biodegradation of Ag Nanoparticles, Storage in Ferritin, and Protection by a Au Shell for Enhanced Photothermal Therapy. *ACS Nano* **2018**, *12* (7), 6523-6535. DOI: 10.1021/acsnano.8b00482
(25) Zhu, L.; Pelaz, B.; Chakraborty, I.; Parak, W. J. Investigating Possible Enzymatic Degradation on Polymer Shells around Inorganic Nanoparticles. *Int J Mol Sci* **2019**, *20* (4). DOI: 10.3390/ijms20040935
(26) Fernández-Afonso, Y.; Asín, L.; Beola, L.; Fratila, R. M.; Gutiérrez, L. Influence of Magnetic Nanoparticle Degradation in the Frame of Magnetic Hyperthermia and Photothermal Treatments. *ACS Applied Nano Materials* **2022**, *5* (11), 16220-16230. DOI: 10.1021/acsanm.2c03220
(27) Plan Sangnier, A.; Van de Walle, A. B.; Curcio, A.; Le Borgne, R.; Motte, L.; Lalatonne, Y.; Wilhelm, C. Impact of magnetic nanoparticle surface coating on their long-term intracellular biodegradation in stem cells. *Nanoscale* **2019**, *11* (35), 16488-16498, 10.1039/C9NR05624F. DOI: 10.1039/C9NR05624F
(28) Portilla, Y.; Fernández-Afonso, Y.; Pérez-Yagüe, S.; Mulens-Arias, V.; Morales, M. P.; Gutiérrez, L.; Barber, D. F. Different coatings on magnetic nanoparticles dictate their degradation kinetics in vivo for 15 months after intravenous administration in mice. *Journal of Nanobiotechnology* **2022**, *20* (1), 543. DOI: 10.1186/s12951-022-01747-5
(29) Krętowski, R.; Kusaczuk, M.; Naumowicz, M.; Kotyńska, J.; Szynaka, B.; Cechowska-Pasko, M. The Effects of Silica Nanoparticles on Apoptosis and Autophagy of Glioblastoma Cell Lines. *Nanomaterials* **2017**, *7* (8), 230.
(30) Boitard, C.; Curcio, A.; Rollet, A.-L.; Wilhelm, C.; Ménager, C.; Griffete, N. Biological Fate of Magnetic Protein-Specific Molecularly Imprinted Polymers: Toxicity and Degradation. *ACS Applied Materials & Interfaces* **2019**, *11* (39), 35556-35565. DOI: 10.1021/acsami.9b11717
(31) Habault, D.; Dery, A.; Leng, J.; Lecommandoux, S.; Meins, J. F. L.; Sandre, O. Droplet Microfluidics to Prepare Magnetic Polymer Vesicles and to Confine the Heat in Magnetic Hyperthermia. *IEEE Transactions on Magnetics* **2013**, *49* (1), 182-190. DOI: 10.1109/TMAG.2012.2221688

(32) Robb, M. J.; Connal, L. A.; Lee, B. F.; Lynd, N. A.; Hawker, C. J. Functional block copolymer nanoparticles: toward the next generation of delivery vehicles. *Polymer Chemistry* **2012**, *3* (6), 1618-1628, 10.1039/C2PY20131C. DOI: 10.1039/C2PY20131C
(33) Lecommandoux, S.; Sandre, O.; Chécot, F.; Rodriguez-Hernandez, J.; Perzynski, R. Self-assemblies of magnetic nanoparticles and di-block copolymers: Magnetic micelles and vesicles. *Journal of Magnetism and Magnetic Materials* **2006**, *300* (1), 71-74. DOI: https://doi.org/10.1016/j.jmmm.2005.10.035
(34) Berret, J.-F.; Schonbeck, N.; Gazeau, F.; El Kharrat, D.; Sandre, O.; Vacher, A.; Airiau, M. Controlled Clustering of Superparamagnetic Nanoparticles Using Block Copolymers: Design of New Contrast Agents for Magnetic Resonance Imaging. *Journal of the American Chemical Society* **2006**, *128* (5), 1755-1761. DOI: 10.1021/ja0562999
(35) Hickey, R. J.; Haynes, A. S.; Kikkawa, J. M.; Park, S.-J. Controlling the Self-Assembly Structure of Magnetic Nanoparticles and Amphiphilic Block-Copolymers: From Micelles to Vesicles. *Journal of the American Chemical Society* **2011**, *133* (5), 1517-1525. DOI: 10.1021/ja1090113
(36) Mai, Y.; Eisenberg, A. Self-assembly of block copolymers. *Chemical Society Reviews* **2012**, *41* (18), 5969-5985, 10.1039/C2CS35115C. DOI: 10.1039/C2CS35115C
(37) Vilsinski, B. H.; Witt, M. A.; Barbosa, P. M.; Montanha, M. C.; Nunes, C. S.; Bellettini, I. C.; de Castro, L. V.; Sato, F.; Baesso, M. L.; Muniz, E. C.; et al. Formulation of chloroaluminum phthalocyanine incorporated into PS-b-PAA diblock copolymer nanomicelles. *Journal of Molecular Liquids* **2018**, *271*, 949-958. DOI: https://doi.org/10.1016/j.molliq.2018.09.034
(38) Vyhnalkova, R.; Eisenberg, A.; van de Ven, T. G. M. Loading and Release Mechanisms of a Biocide in Polystyrene-Block-Poly(acrylic acid) Block Copolymer Micelles. *The Journal of Physical Chemistry B* **2008**, *112* (29), 8477-8485. DOI: 10.1021/jp8009707
(39) Benassai, E.; Hortelao, A. C.; Aygun, E.; Alpman, A.; Wilhelm, C.; Saritas, E. U.; Abou-Hassan, A. High-throughput large scale microfluidic assembly of iron oxide nanoflowers@PS-b-PAA polymeric micelles as multimodal nanoplatforms for photothermia and magnetic imaging. *Nanoscale Advances* **2024**, *6* (1), 126-135, 10.1039/D3NA00700F. DOI: 10.1039/D3NA00700F
(40) del Monte, F.; Morales, M. P.; Levy, D.; Fernandez, A.; Ocaña, M.; Roig, A.; Molins, E.; O'Grady, K.; Serna, C. J. Formation of γ-Fe2O3 Isolated Nanoparticles in a Silica Matrix. *Langmuir* **1997**, *13* (14), 3627-3634. DOI: 10.1021/la9700228
(41) Haddad, P. S.; Duarte, E. L.; Baptista, M. S.; Goya, G. F.; Leite, C. A.; Itri, R. Synthesis and characterization of silica-coated magnetic nanoparticles. In *Surface and Colloid Science*, Springer, 2004; pp 232-238.
(42) Lojk, J.; Bregar, V. B.; Rajh, M.; Miš, K.; Kreft, M. E.; Pirkmajer, S.; Veranič, P.; Pavlin, M. Cell type-specific response to high intracellular loading of polyacrylic acid-coated magnetic nanoparticles. *International journal of nanomedicine* **2015**, *10*, 1449-1462. DOI: 10.2147/IJN.S76134

(43) Wahsner, J.; Gale, E. M.; Rodríguez-Rodríguez, A.; Caravan, P. Chemistry of MRI Contrast Agents: Current Challenges and New Frontiers. *Chemical Reviews* **2019**, *119* (2), 957-1057. DOI: 10.1021/acs.chemrev.8b00363
(44) Eichhorn, J.; Gordievskaya, Y. D.; Kramarenko, E. Y.; Khokhlov, A. R.; Schacher, F. H. pH-Dependent Structure of Block Copolymer Micelles Featuring a Polyampholyte Corona: A Combined Experimental and Theoretical Approach. *Macromolecules* **2021**, *54* (4), 1976-1991. DOI: 10.1021/acs.macromol.0c02344
(45) Kuiper, P.; Searle, B. G.; Duda, L. C.; Wolf, R. M.; van der Zaag, P. J. Fe L2,3 linear and circular magnetic dichroism of Fe3O4. *Journal of Electron Spectroscopy and Related Phenomena* **1997**, *86* (1), 107-113. DOI: https://doi.org/10.1016/S0368-2048(97)00053-4
(46) Carvallo, C.; Sainctavit, P.; Arrio, M.-A.; Menguy, N.; Wang, Y.; Ona-Nguema, G.; Brice-Profeta, S. Biogenic vs. abiogenic magnetite nanoparticles: A XMCD study. *American Mineralogist* **2008**, *93* (5-6), 880-885. DOI: 10.2138/am.2008.2713
(47) Lee, Y.; Lee, J.; Bae, C. J.; Park, J.-G.; Noh, H.-J.; Park, J.-H.; Hyeon, T. Large-Scale Synthesis of Uniform and Crystalline Magnetite Nanoparticles Using Reverse Micelles as Nanoreactors under Reflux Conditions. *Advanced Functional Materials* **2005**, *15* (3), 503-509. DOI: https://doi.org/10.1002/adfm.200400187
(48) Gilbert, B.; Katz, J. E.; Denlinger, J. D.; Yin, Y.; Falcone, R.; Waychunas, G. A. Soft X-ray Spectroscopy Study of the Electronic Structure of Oxidized and Partially Oxidized Magnetite Nanoparticles. *The Journal of Physical Chemistry C* **2010**, *114* (50), 21994-22001. DOI: 10.1021/jp106919a
(49) Coker, V. S.; Pearce, C. I.; Lang, C.; van der Laan, G.; Pattrick, R. A. D.; Telling, N. D.; Schüler, D.; Arenholz, E.; Lloyd, J. R. Cation site occupancy of biogenic magnetite compared to polygenic ferrite spinels determined by X-ray magnetic circular dichroism. *European Journal of Mineralogy* **2007**, *19* (5), 707-716. DOI: 10.1127/0935-1221/2007/0019-1758
(50) Guyodo, Y.; Sainctavit, P.; Arrio, M.-A.; Carvallo, C.; Lee Penn, R.; Erbs, J. J.; Forsberg, B. S.; Morin, G.; Maillot, F.; Lagroix, F.; et al. X-ray magnetic circular dichroïsm provides strong evidence for tetrahedral iron in ferrihydrite. *Geochemistry, Geophysics, Geosystems* **2012**, *13* (6). DOI: https://doi.org/10.1029/2012GC004182
(51) Everett, J.; Brooks, J.; Lermyte, F.; O'Connor, P. B.; Sadler, P. J.; Dobson, J.; Collingwood, J. F.; Telling, N. D. Iron stored in ferritin is chemically reduced in the presence of aggregating Aβ(1-42). *Scientific Reports* **2020**, *10* (1), 10332. DOI: 10.1038/s41598-020-67117-z

Table of contents

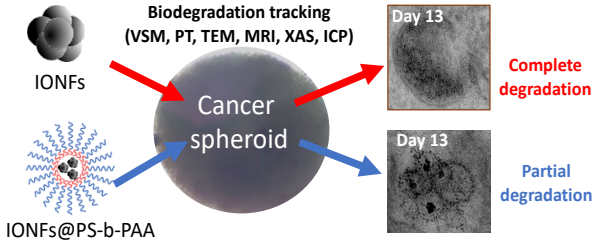
Biodegradation tracking
(VSM, PT, TEM, MRI, XAS, ICP)
IONFs
Cancer spheroid
IONFs@PS-b-PAA
Day 13
Complete degradation
Day 13
Partial degradation